Hydrogenated V_2O_5 with Improved Optical and Electrochemical Activities for Photo-accelerated Lithium-ion Batteries

Yinan Lu,[1] Holly Andersen,[1] Ruiqi Wu,[2] Alex M. Ganose,[2] Bo Wen,[3] Arvind Pujari,[3,4] Tianlei Wang,[5] Joanna Borowiec,[5] Ivan P. Parkin,[5,*] Michael De Volder,[3,*] and Buddha Deka Boruah[1,*]

[1]Institute for Materials Discovery, University College London, London WC1E 7JE, United Kingdom

[2]Department of Chemistry, Molecular Sciences Research Hub, White City Campus, Imperial College London, Wood Lane, London, United Kingdom

[3]Institute for Manufacturing, Department of Engineering, University of Cambridge, Cambridge CB3 0FS, United Kingdom

[4]Cavendish Laboratory, Department of Physics, University of Cambridge, Cambridge CB3 0HE, United Kingdom

[5]Department of Chemistry, University College London, London WC1H 0AJ, United Kingdom

*Corresponding authors: Prof. Ivan P. Parkin – i.p.parkin@ucl.ac.uk

Prof. Michael De Volder – mfld2@cam.ac.uk

Dr. Buddha Deka Boruah – b.boruah@ucl.ac.uk

Abstract

Solar power represents an abundant and readily available source of renewable energy. However, its intermittent nature necessitates external energy storage solutions, which can often be expensive, bulky, and associated with energy conversion losses. Our study introduces the concept of a photo-accelerated battery that seamlessly integrates energy harvesting and storage functions within a single device. In this research, we present a novel approach for crafting photocathodes using hydrogenated vanadium pentoxide ($H:V_2O_5$) nanofibers. This method enhances optical activity, electronic conductivity, and ion diffusion rates within photo-accelerated Li-ion batteries. Our findings reveal that $H:V_2O_5$ exhibits notable improvements in specific capacity under both dark and illuminated conditions. Furthermore, it demonstrates enhanced diffusion kinetics and charge storage performance when exposed to light, as compared to pristine counterparts. This strategy of defect engineering holds great promise for the development of high-performance photocathodes in future energy storage applications.

Keywords: Photo-accelerated batteries, lithium-ion batteries, hydrogenated vanadium pentoxide, photocathodes.

Introduction

The 21st century is marked by a growing demand for energy and an urgent need to shift towards renewable energy sources, driven by the detrimental environmental effects of fossil fuels. Energy scarcity has thus become a prominent global concern. While wind and solar power offer sustainable energy solutions, their intermittent availability requires the incorporation of energy storage components to ensure a continuous energy supply. The conventional approach involves connecting photovoltaic cells to external energy storage devices.[1] However, this approach presents challenges such as increased ohmic resistance and energy mismatch between components, resulting in suboptimal energy harvesting efficiency, elevated costs, and added bulk and weight.[2, 3] To address these challenges, researchers propose the development of photo-accelerated batteries that seamlessly integrate energy harvesting and storage capabilities within a single device. This innovative approach has the potential to reduce costs, enhance conversion efficiency, and yield compact and lightweight devices. Such devices find promising applications in fields like wearable technology and the Internet of Things. To achieve the desired performance, the photoelectrode material must serve as a dual-functional semiconductor, capable of simultaneously absorbing light and storing electrochemical energy. It should also minimize charge recombination and improve the conduction of photo-generated charges.[4, 5] Furthermore, it must facilitate rapid ion transport during insertion and de-insertion, preserving efficient diffusion pathways.[6]

To date, the primary focus of research in the field of photo-accelerated energy storage has predominantly centered on lithium-ion battery (LIB) systems. This preference is attributable to LIB's exceptional attributes, such as high energy density, lightweight nature, and extended cycle life.[7-9] Within this context, vanadium pentoxide (V_2O_5) has garnered considerable attention as a potential cathode material for LIBs. Its appeal lies in its cost-effectiveness, abundant availability, ease of controlling its morphology, and substantial theoretical capacity

for Li^+ intercalation. Numerous studies have explored V_2O_5 as a photocathode material, and notable among them is Wang et al., who employed LiV_2O_5 as a photocathode in photo-accelerated LIBs. Their efforts yielded a noteworthy specific capacity of 185 mAh g^{-1} under illumination, representing a substantial 270% improvement over the capacity achieved in the absence of light.[10] We have also delved into the utilization of V_2O_5 photocathodes for photo-accelerated LIBs, showcasing enhancements in charge storage performance when exposed to light.[11]

This investigation employs a defect engineering strategy involving the hydrogenation of V_2O_5 ($H:V_2O_5$) nanofibers to augment the performance of photocathodes in photo-accelerated lithium-ion batteries (LIBs). The electrodes are fabricated by blending V_2O_5 nanofibers with reduced graphene oxide (rGO) and poly(3-hexylthiophene) (P3HT), yielding a heterojunction structure designed to facilitate the separation and conduction of photo-generated charges. Hydrogenation is leveraged to introduce oxygen defects and oxygen-containing hydroxyl groups into the V_2O_5, thereby enhancing material conductivity, photo-response when exposed to light, and ion diffusion rates. Consequently, these enhancements culminate in improved electrochemical energy storage performance. Notably, the $H:V_2O_5$ photocathodes exhibit superior performance compared to pristine V_2O_5 under both illuminated and dark conditions. This study underscores the efficacy of the defect engineering approach in tailoring photocathode material properties to boost photo-accelerated performance, laying a foundation for future developments in photocathode design.

Results and Discussion

The V_2O_5 nanofibers, synthesized via the hydrothermal process, exhibit diameters within the range of 20 to 150 nm, as illustrated in **Figure 1a**. Further insights into the nanofiber structure are provided by the transmission electron microscopy (TEM) and high-resolution TEM

(HRTEM) images displayed in **Figure 1b** and **c**. Notably, the measured d-spacing is 0.218 nm, corresponding to the (002) planes, as depicted in **Figure 1d**. Following thermal treatment under a hydrogen and helium environment at 200 °C for a duration of 2 hours, the H:V_2O_5 samples maintain the same nanofiber morphology as the pristine V_2O_5, as evident from the scanning electron microscope (SEM) and TEM images in **Figure 1e** and **f**. HRTEM analysis (**Figure 1g, h**) reveals a calculated d-spacing of 0.289 nm, corresponding to the (301) planes. Additionally, **Figure S1** provides the respective selected area electron diffraction (SAED) patterns for both the V_2O_5 and H:V_2O_5 samples, confirming the preservation of the orthorhombic V_2O_5 crystal structure in both the pristine and hydrogenated samples. This structural integrity is further corroborated by the X-ray diffraction (XRD) patterns shown in **Figure 1i**, with a space group of Pmmn (59) and JCPDS card no: 03-065-0131. It's worth noting that elevating the hydrogenation temperature of V_2O_5 to 300 °C results in the formation of a monoclinic VO_2 phase, as reported in previous studies.[12] Therefore, to maintain the morphology and crystallinity of pristine V_2O_5, the hydrogenation temperature was held at 200 °C. Additionally, the Raman spectra (**Figure 1j**) of both the pristine and hydrogenated samples show the same Raman shifts at approximately 994 cm^{-1}, 484 cm^{-1}, and 405 cm^{-1} related to the stretching vibration of the vanadyl bond (V=O) and the symmetric stretching of V–$O_{(3)}$–V, and the angle-bending of V–$O_{(3)}$–V. Peaks centered at approximately 701 cm^{-1}, 526 cm^{-1}, 304 cm^{-1}, and 284 cm^{-1} are assigned to the stretching of V–O–V bonds, the V_3O phonon band, the bending vibration of V–O_C, and the bond bending vibration of O_C–V–O_B. The additional Raman shift at approximately 197 cm^{-1} corresponds to the bending vibration of the O_C–V–O_B (A_g mode) bond.[13] The normalized V 2p3 spectra (**Figure 1k**) of the samples showed identical characteristic peaks related to V $2p_{1/2}$ (~524.6 eV) and V $2p_{3/2}$ (~517.2 eV). The X-ray photoelectron spectroscopy (XPS) spectra of O1s (depicted in **Figure 1l**) reveal distinct features. Specifically, a prominent characteristic peak is observed at approximately 529.8 eV,

corresponding to lattice oxygen (V-O). Additionally, in the hydrogenated sample, an extra broad peak emerges at approximately 532 eV. This additional peak arises due to the presence of both oxygen vacancies and oxygen-containing hydroxyl groups (-OH) following the hydrogenation process. This observation aligns with previous reports.[14-17] Similarly, the energy-dispersive X-ray spectroscopy (EDS) mappings (as shown in **Figure S2**) also indicate a reduction in oxygen content after hydrogenation. Specifically, the atomic percentage (At%) ratio shifts from 67:33 (O:V) in pristine V_2O_5 to 64.9:35.1 (O:V) after the hydrogenation of V_2O_5. In contrast, the H:V_2O_5 sample displays broader absorption in its UV-Vis spectrum (**Figure 1m**) compared to pristine V_2O_5. This broadening is attributed could be due to the creation of defect states. The inset in **Figure 1m** depicts the photoluminescence (PL) spectra, which show an increase in the intensity of the broad peak associated with mid-gap states between the valence band and conduction band of V_2O_5 formed by defect states following hydrogenation.[18, 19]

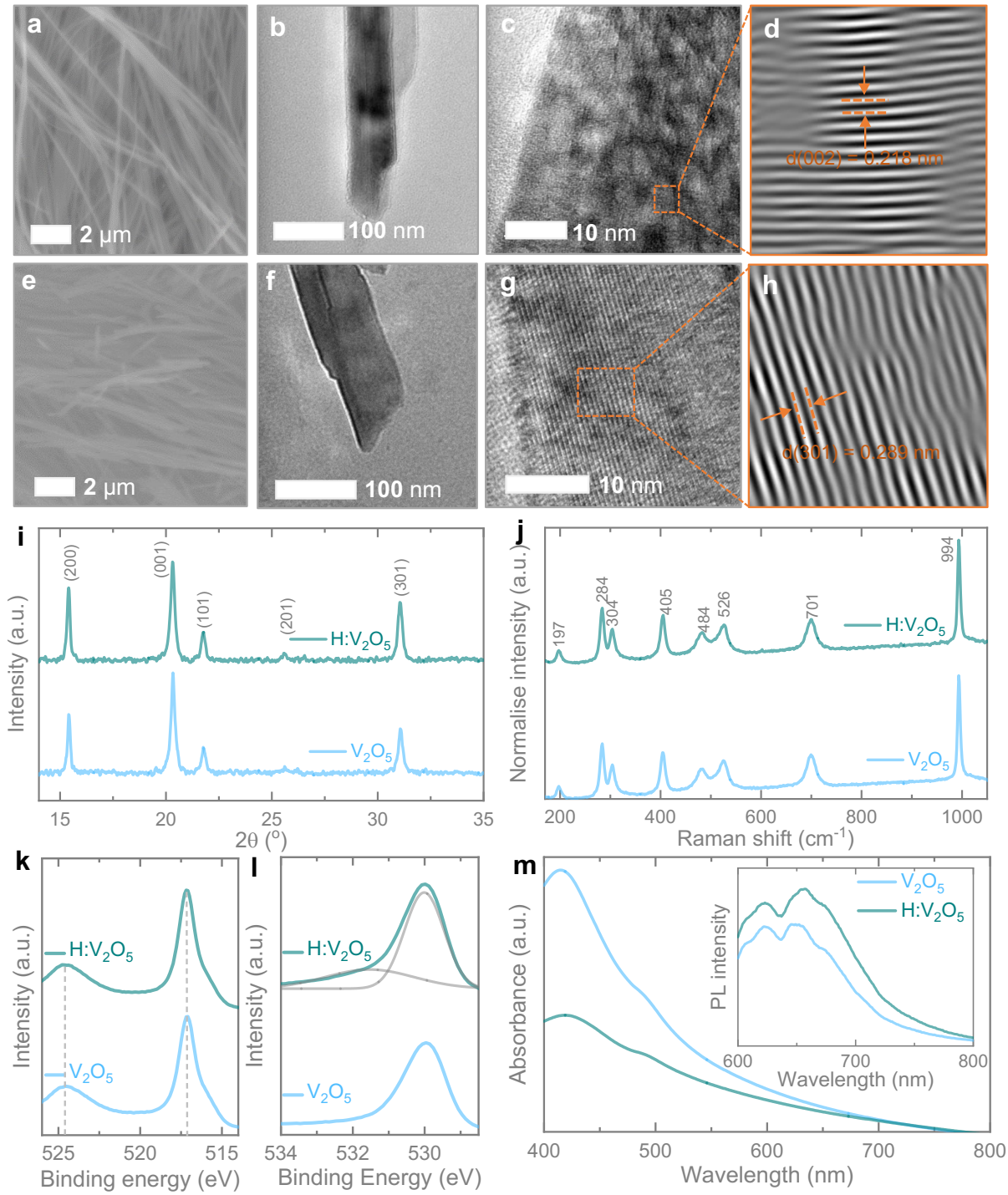

Figure 1. *SEM, TEM and HRTEM images of (a-d) V_2O_5 and (e-h) H:V_2O_5. (i) XRD patterns and (j) Raman spectra of V_2O_5 and H:V_2O_5 confirm orthorhombic V_2O_5 crystal structure. (k, l) V 2p3 high-resolution and O 1s high-resolution XPS spectra of V_2O_5 and H:V_2O_5. (m) UV-Vis spectra of V_2O_5 and H:V_2O_5. Inset in (m) shows the PL spectra of the samples.*

To examine the electrical photo-responses of our samples, we initially designed photodetectors with metal-semiconductor-metal interdigitated electrodes (IDEs) (**Figure S3** provides a visual representation). These photodetectors were constructed using gold (Au) with either V_2O_5 or H:V_2O_5. To ensure a fair comparison of the electrical and photo-responses between V_2O_5 and H:V_2O_5, we applied equal amounts of these materials to identical Au IDEs. Subsequently, we measured the current-voltage characteristics of these photodetectors under both dark and illuminated conditions (depicted in **Figures 2a** and **b**). Our observations revealed an increase in current when the photodetectors were exposed to light for both V_2O_5 and H:V_2O_5, affirming the photosensitive nature of these materials. Importantly, we noted that the hydrogenated samples exhibited higher currents under both dark and illuminated conditions. This finding suggests that the hydrogenation process enhances both the electrical conductivity and optical activity of the materials. Following the hydrogenation process of V_2O_5, the presence of both oxygen vacancies and oxygen-containing hydroxyl groups (-OH) occurs. This leads to the formation of defect states located within the mid-gap region, which lies in the forbidden band gap.[18,19] Some of the free electrons may migrate to the conduction band, generating free charges that contribute to improved electrical conductivity. Furthermore, we conducted comparative response current measurements (defined as photo-current minus dark current) over time under alternating dark and light conditions, maintaining a bias voltage of 1 V. These measurements further validated the superior photo-responses of the hydrogenated samples compared to the pristine samples (**Figure 2c**).

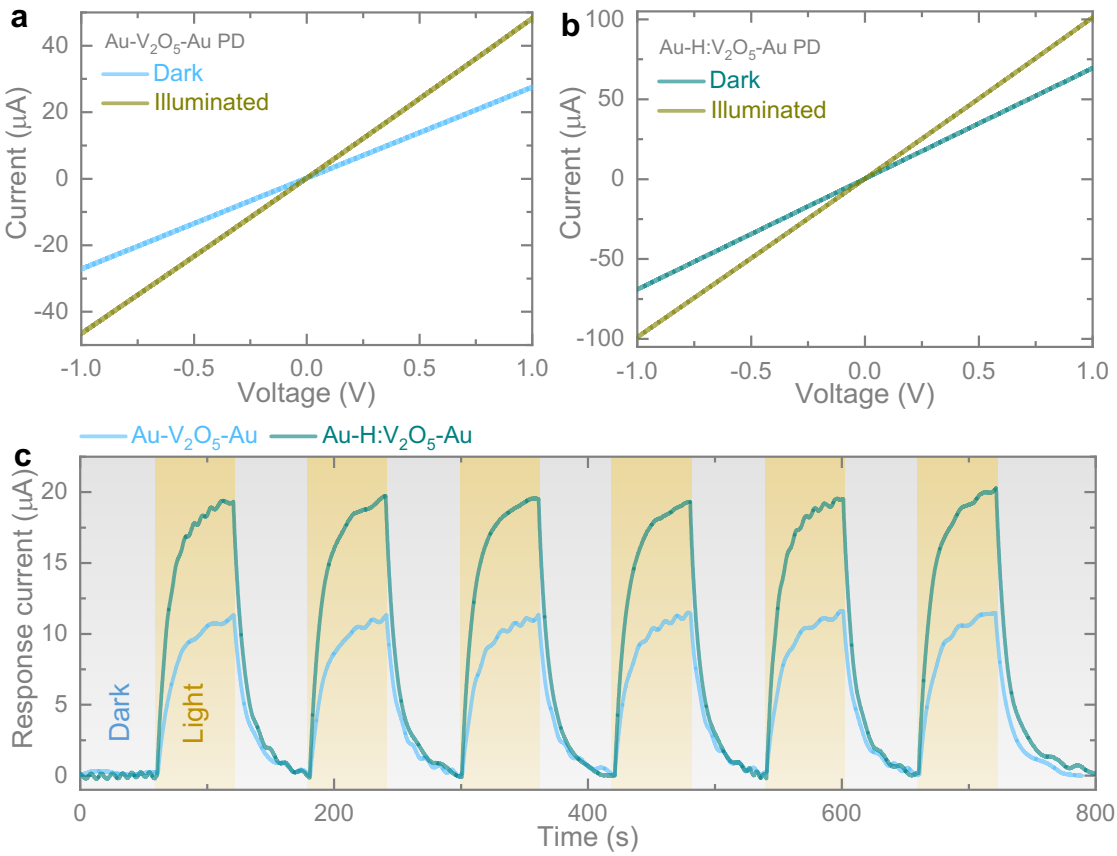

Figure 2. *Current-volage responses of the (a) V_2O_5 and (b) H:V_2O_5 photodetectors in dark and illuminated conditions. (c) Response current-time curves of the photodetectors under alternating dark and light cycles at a bias voltage of 1 V.*

The lithium-ion storage characteristics of our samples were investigated using an optical cell of CR2032 coin cell type, featuring a 7 mm optical window for light exposure, configured in a half-cell arrangement (refer to **Figure S4** for a visual representation of the optical cell). To create photocathodes, we prepared a mixture of materials (either V_2O_5 or H:V_2O_5) with rGO, P3HT, and polyvinylidene fluoride (PVDF) in a ratio of 91:2:2:5 (details provided in the experimental section, Supporting Information). We recorded cyclic voltammograms (CVs) for both pristine and hydrogenated samples at various scan rates ranging from 0.1 to 1.0 mV s^{-1}, within a potential range spanning from 2.0 V to 4.0 V (as depicted in **Figures 3a** and **b**). The intercalation process of Li^+ into V_2O_5 involves multiple phase transitions, contingent upon the

degree of Li^+ intercalation, giving rise to distinct redox couples. These redox processes manifest as cathodic peaks, which are centered at approximately 3.33 V, 3.12 V, and 2.28 V, corresponding to the transformation of V_2O_5 from its α-phase to the ε-phase, δ-phase, and γ-phase, respectively. Similarly, corresponding anodic peaks are centered at approximately 2.58 V, 3.36 V, and 3.51 V.[20] Interestingly, the hydrogenated samples exhibited higher peak currents, both for cathodic and anodic peaks, when compared to pristine V_2O_5. This observation indicates an enhancement in lithium-ion storage capacity following the hydrogenation process.

Figures 3c and **d** provide a visual representation of the differences in cyclic voltammograms (CVs) at scan rates of 0.5 mV s^{-1} and 1.0 mV s^{-1}. These figures illustrate a significant increase in the CV area of approximately 34% (at 0.5 mV s^{-1}) and approximately 36.7% (at 1.0 mV s^{-1}) as a result of hydrogenation. Furthermore, **Figure S5** in the Supporting Information presents comparative CVs at scan rates of 0.1 mV s^{-1}, 0.2 mV s^{-1}, 0.6 mV s^{-1}, and 0.8 mV s^{-1}, demonstrating a notable enhancement in the respective redox peaks following hydrogenation. The peak current (i_p) observed in the CV curves can be related to the diffusion constant (D) of Li-ions using the equation: $i_p = 0.4463F(F/RT)^{1/2}ACD^{1/2}v^{1/2} = KD^{1/2}v^{1/2}$. In this equation, T represents the cell testing temperature, F is the Faraday constant, C denotes the initial Li-ion molar concentration in the electrolyte, R is the gas constant, and A represents the electrode area.[21] By maintaining a constant electrode area for both pristine and hydrogenated samples, the slope of i_p/K *vs.* $v^{1/2}$ from the mentioned equation can estimate the diffusion constant. **Figures 3e** and **f** display the plots of i_p/K *vs.* $v^{1/2}$ for the C1 (~ -3.33 V)/A1 (~3.36 V) and C2 (~ -3.12 V)/A2 (~3.51 V) peaks, respectively. The calculated enhancements in the diffusion constant amount to 55.12% (C1) and 49.19% (C2) for the cathodic peaks and 39.82% (A1) and 43.48% (A2) for the anodic peaks after hydrogenation.

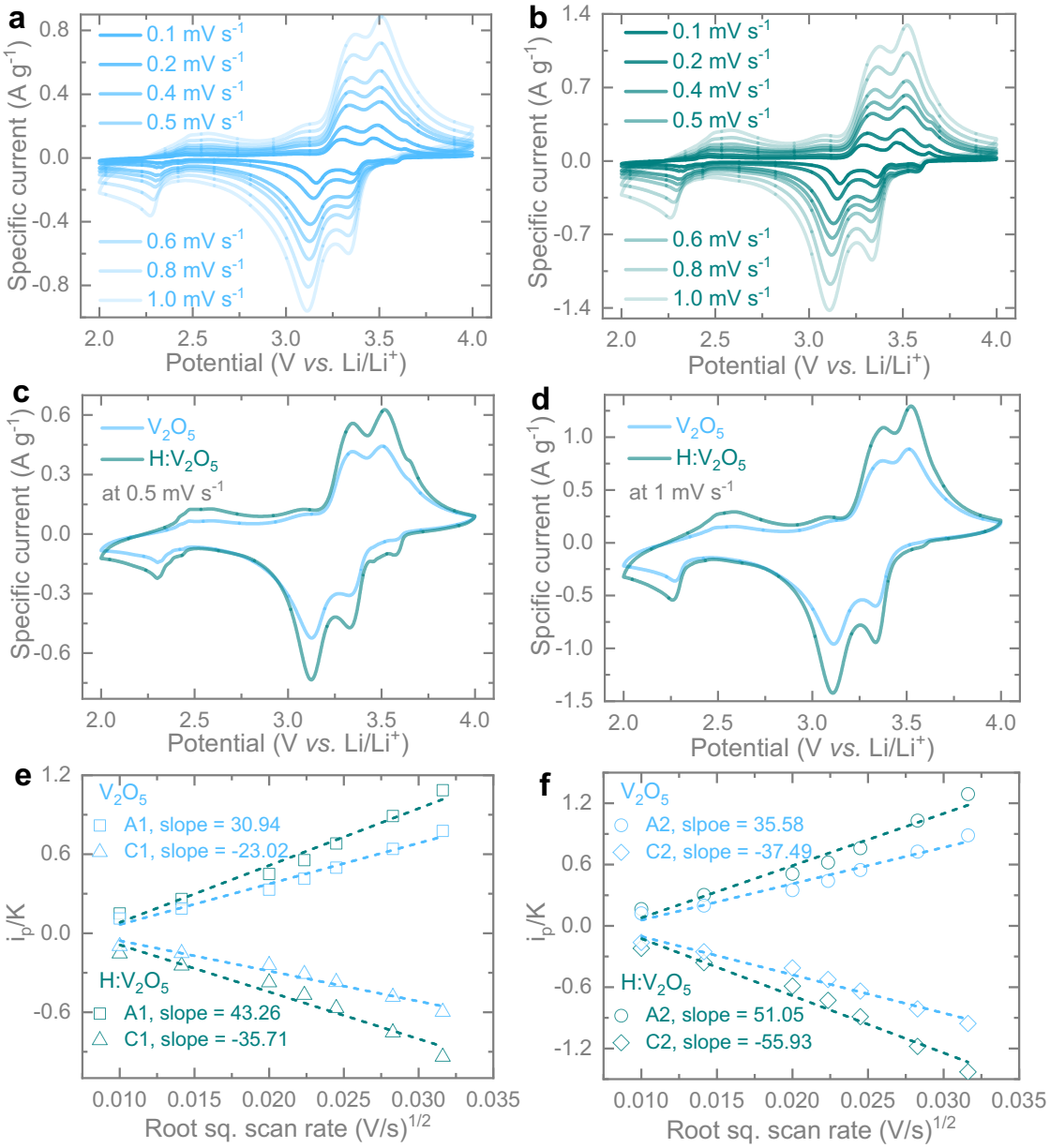

Figure 3. *CV curves of the (a) V_2O_5 and (b) H:V_2O_5 at different scans (0.1 – 1.0 mV s^{-1}) in the dark. Comparative CVs of V_2O_5 and H:V_2O_5 at scan rates of (c) 0.5 mV s^{-1} and (d) 1.0 mV s^{-1} in dark conditions. (e, f) i_p/K vs. $v^{1/2}$ plots for C1 (~3.33 V)/A1 (~3.36 V) and C2 (~3.12 V)/A2 (~3.51 V) peaks.*

To gain deeper insights into the impact of light on these materials, we performed CV measurements on both the pristine and hydrogenated samples under illumination with light at a wavelength of approximately 455 nm and an intensity of around 12 mW cm^{-2}. **Figure S6** in

the Supporting Information presents the CVs of H:V_2O_5 at various scan rates (ranging from 0.1 mV s^{-1} to 1.0 mV s^{-1}) under illumination. The comparative CVs of H:V_2O_5 at scan rates of 0.5 mV s^{-1}, 0.8 mV s^{-1}, and 1.0 mV s^{-1}, as depicted in **Figures 4a-c**, clearly illustrate an enhancement in charge storage performance under illumination. Specifically, there is an increase of approximately 47.4% (at 0.5 mV s^{-1}) and 46.7% (at 1.0 mV s^{-1}) in the enclosed CV areas compared to measurements conducted in the dark. This substantial improvement in Li^+ ion storage performance under illumination is attributed to the enhanced optical activity resulting from hydrogenation. Moreover, when comparing the CVs of H:V_2O_5 and V_2O_5 at a scan rate of 0.5 mV s^{-1} (**Figure 4d)**, H:V_2O_5 exhibits approximately 61.3% higher CV areas even under illumination. Additionally, **Figure 4e** reveals that the calculated enhancements in diffusion constants amount to approximately 43.7% (C1), 50.9% (A1), 59.5% (C2), and 35.8% (A2) after hydrogenation, compared to their respective pristine counterparts under illuminated conditions (**Table S1** presents the slopes of the corresponding cathodic and anodic peaks). These findings further confirm the improved Li^+ ion diffusion kinetics after hydrogenation in both dark and illuminated conditions. Furthermore, under light illumination, there is a notable enhancement in Li^+ ion diffusion kinetics for H:V_2O_5 compared to the dark conditions. Specifically, the estimated enhancements are approximately 27.33% and 48.2% for the cathodic peaks C1 and C2, respectively, and 55.2% and 15.8% for the anodic peaks A1 and A2 (**Figure 4f**).

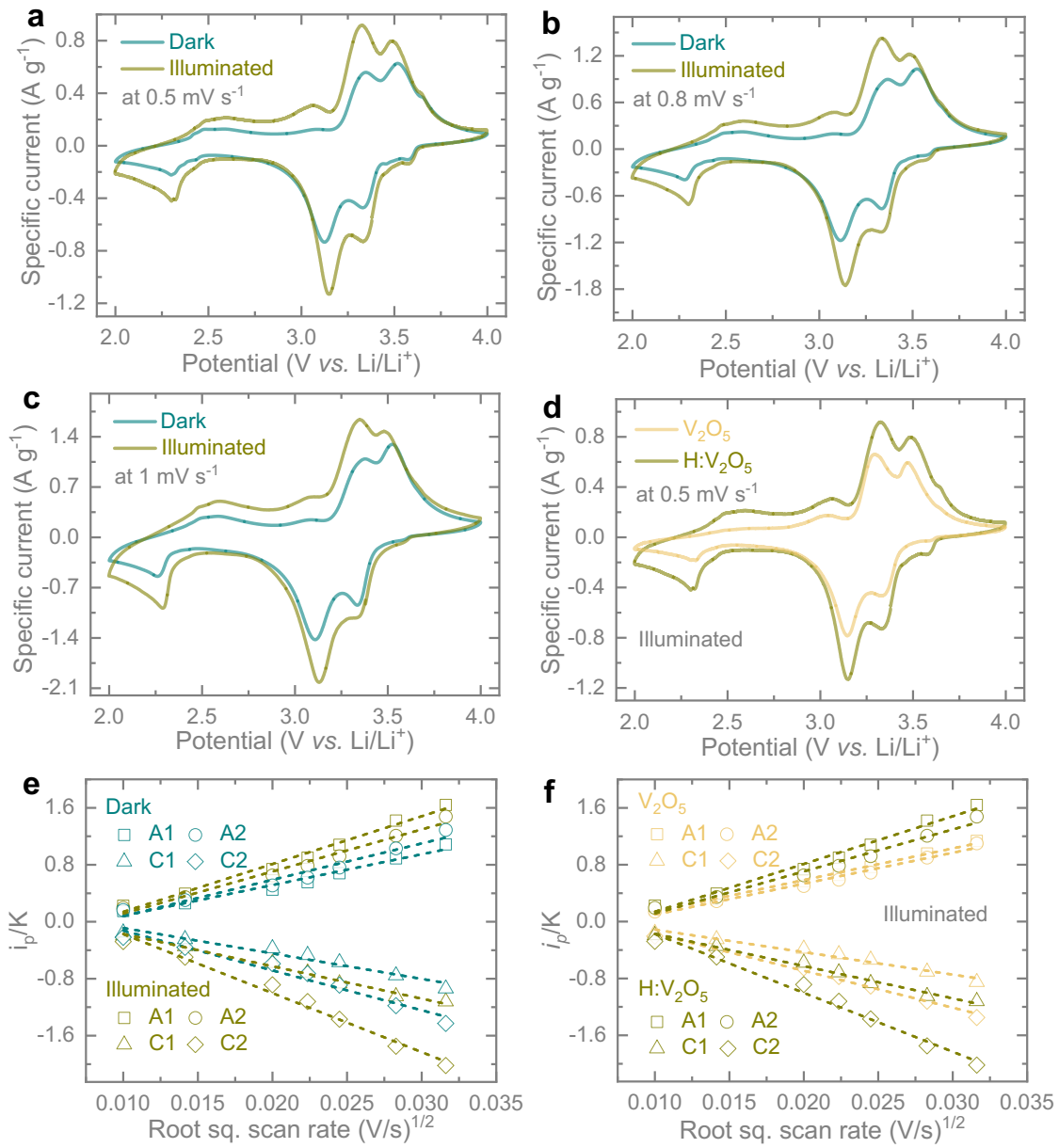

Figure 4. *CV curves of H:V_2O_5 at scan rates of (a) 0.5 mV s^{-1}, (b) 0.8 mV s^{-1} and (b) 1 mV s^{-1} in dark and illuminated conditions. (d) Comparative CVs at 0.5 mV s^{-1} of V_2O_5 and H:V_2O_5 in illuminated conditions. (e) Diffusion constant analysis of H:V_2O_5 in dark and illuminated conditions. (f) Diffusion constant analysis of V_2O_5 and H:V_2O_5 in illuminated conditions.*

Furthermore, we conducted galvanostatic discharge-charge (GDC) tests on both the V_2O_5 and H:V_2O_5 samples under various specific currents, ranging from 200 mA g^{-1} to 2000 mA g^{-1}, over a potential range of 2 V – 4 V (*vs.* Li/Li^+) in both dark and illuminated conditions (with light

at λ ~ 455 nm and intensity ~12 mW cm^{-2}). As expected, in line with the CV results presented in **Figures 3** and **4**, the hydrogenated samples exhibited superior electrochemical responses compared to the pristine sample, irrespective of whether the tests were conducted in the dark or under illumination. This improvement is corroborated by the comparative GDC curves (**Figures 5a** and **b**), which clearly demonstrate an increase in specific capacities. Specifically, the specific capacity increased from 114 mAh g^{-1} to 151 mAh g^{-1} (reflecting a ~32.45% enhancement) at a specific current of 500 mA g^{-1}, and from 63 mAh g^{-1} to 90 mAh g^{-1} (indicating a ~42.85% enhancement) at a specific current of 2000 mA g^{-1} in the dark. Furthermore, the comparative GDC curves of H:V_2O_5 under dark and illuminated conditions (**Figures 5c, d,** and **S7**) substantiate the enhancement in charge storage capacities under illumination compared to the dark. This enhancement is attributed to the involvement of photo-charges in the charge storage process. The extracted *dQ/dV* curves (**Figure 5e**) derived from the GDC tests further support the improvements in Li^+ ion storage observed in the H:V_2O_5 sample compared to the V_2O_5 sample in the dark. Similarly, the *dQ/dV* plots for H:V_2O_5 (**Figure 5f**) indicate the participation of photo-charges in the charge storage process. To illustrate the enhanced electrochemical performance, we can utilize electrochemical impedance spectroscopy (EIS). The Nyquist plots provide valuable insights into the charge transfer resistance, and in the case of H:V_2O_5, it is observed to decrease from 16 **Ω** to 14 **Ω** after hydrogenation under illumination. Additionally, there is a reduction in the equivalent series resistance, as depicted in **Figure S8a**. Moreover, **Figure S8b** reveals that the charge transfer resistance of H:V_2O_5 decreases from 48 **Ω** to 14 **Ω** when comparing illuminated conditions to dark conditions. In **Figure S8c**, we present the equivalent circuit model for the Nyquist plots. These results are consistent with the estimates of the diffusion constants obtained from the CV curves.

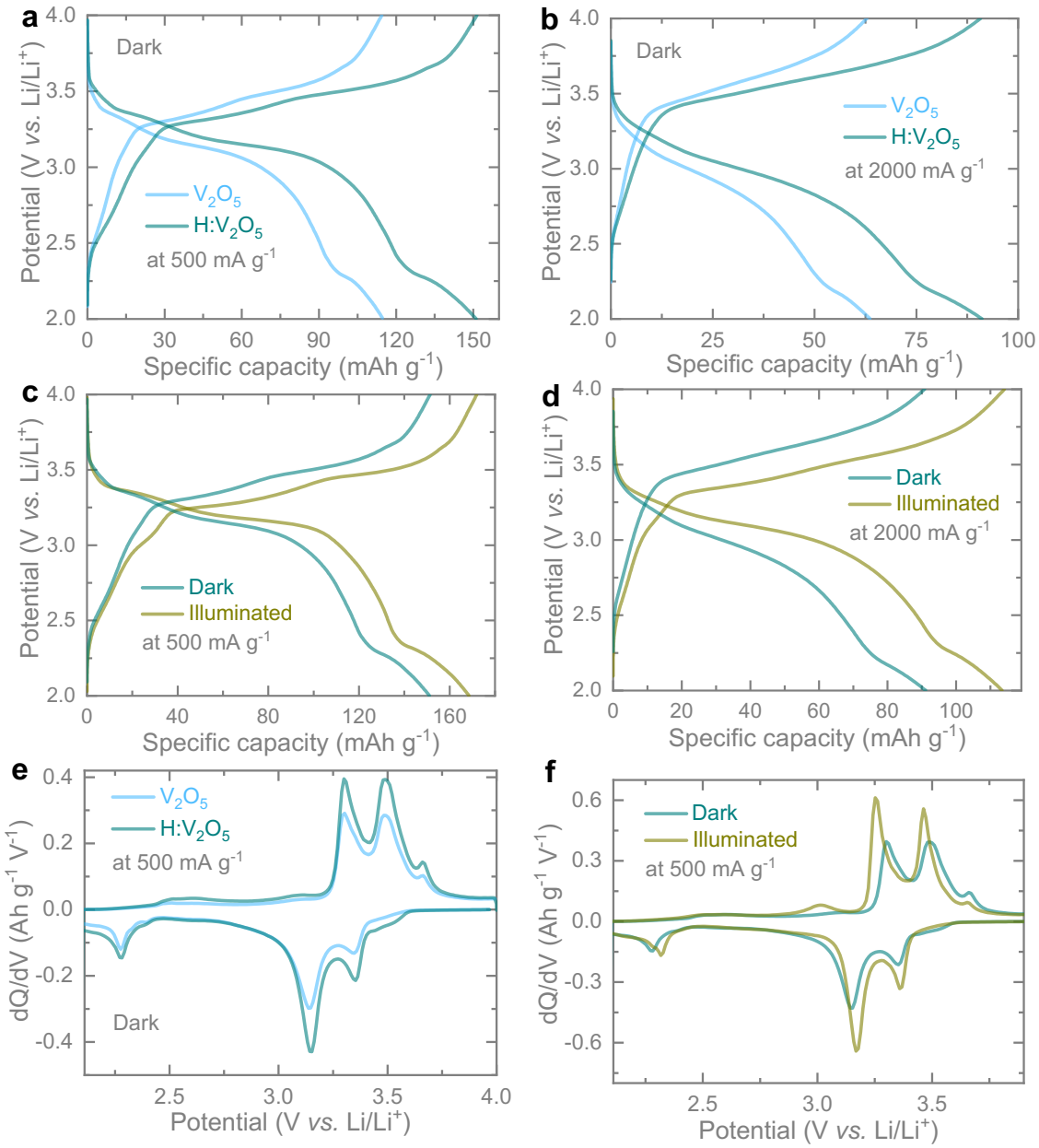

Figure 5. *(a, b) Comparative GDCs of V_2O_5 and $H:V_2O_5$ at specific currents of 500 mA g^{-1} and 2000 mA g^{-1} in the dark. (c, d) GDCs at 500 mA g^{-1} and 2000 mA g^{-1} of $H:V_2O_5$ in dark and illuminated conditions. (e) dQ/dV curves of V_2O_5 and $H:V_2O_5$ at a specific current of 500 mA g^{-1} in dark. (f) dQ/dV curves of $H:V_2O_5$ at 500 mA g^{-1} in dark and illuminated conditions.*

Furthermore, when conducting rate tests in dark conditions (Figure 6a), significant capacity improvements were observed for both V_2O_5 and $H:V_2O_5$ following hydrogenation at all specific currents. Additionally, under light illumination (**Figure 6b**), $H:V_2O_5$ exhibited capacity enhancements compared to dark conditions at each specific current, attributed to the

participation of photo-charges in the charge storage process. Moreover, **Figure S9** illustrates extended cycling experiments at a specific current of 500 mA g^{-1} for H:V_2O_5 under both dark and illuminated conditions. Notably, after 50 cycles, a significantly improved capacity of 143 mAh g^{-1} was achieved under illumination, while a capacity of 122 mAh g^{-1} was observed under dark conditions during the same cycle test at 500 mA g^{-1}. This underscores the remarkable capacity stability of the hydrogenated sample, which maintains a higher capacity even under illumination compared to dark conditions. The detailed process of charge and photo-charge transfer can be found in our earlier reports.[11, 22] In summary, when exposed to light during the discharge process, photogenerated electrons migrate from V_2O_5 to the CF current collector via the charge transfer materials P3HT and rGO. This movement follows favourable energy pathways and travel to combine with Li^+ ions that migrate from the oxidation reaction at the Li anode. Simultaneously, holes are blocked by P3HT and compensate with the electrons from external circuits. Conversely, during the charging process under illumination, the photo-generated holes push away the Li^+ ions within the V_2O_5 photocathodes, leading to the deintercalation of Li^+ ions.[22] At the same time, photogenerated electrons transition from the valence band to the conduction band of the photocathode. With the assistance of an external electrical bias, these photo-generated electrons travel through the external circuit, promoting the reduction reaction at the Li anode. These processes collectively contribute to the enhancement of charge storage performance under illumination. The hydrogenated samples demonstrate heightened photocurrent generation, possibly attributed to the creation of defect mid-gap states situated between V_2O_5's bandgap. These states are associated with oxygen-related defects and hydroxyl groups leading to enhanced optical absorption (as shown in **Figure 1m**), thereby improving photoactivity.[18; 19] Consequently, this enhancement results in superior photo-enhanced capacities compared to pristine V_2O_5. In addition, we recorded the open-circuit potentials (OCPs) of the V_2O_5 and H:V_2O_5 optical cells under illumination and during discharge in the dark (as depicted in **Figure S10**). This data supports the observed increase in discharge capacity following the hydrogenation of V_2O_5. To investigate the contribution of the photothermal effect to the charge storage, we conducted an analysis of the charge storage performance of H:V_2O_5 at various temperatures, ranging from 25 °C to 65 °C (**Figure S11a** presents absolute CV areas at different temperatures). Intriguingly, there was no significant capacity improvement, with only an 11% increase in capacities recorded at 65 °C compared to 25 °C (as seen in **Figure S11b**). This increase is negligible compared to the substantial capacity enhancement of approximately 47% observed under illumination compared to dark conditions (as shown in **Figure 4c**). Furthermore, it's crucial to emphasize that the LED-based light source

used does not generate significant heat even during continuous illumination. Therefore, it can be concluded that the capacity enhancement under illumination is primarily attributed to photocharges rather than a photothermal effect.

To gain a deeper understanding of the enhanced charge storage performance of hydrogenated V_2O_5 in comparison to pristine V_2O_5, we conducted density functional theory (DFT) calculations of Li^+ migration. Our findings reveal that the improvement is largely controlled by -OH species, which play a role in augmenting the charge storage process. **Figure 6c** provides a schematic representation of the crystal structure of V_2O_5, highlighting potential pathways for Li^+ diffusion. For pristine V_2O_5, previous calculations have indicated that diffusion along the channels parallel to the layers (path A in **Figure** 6c) exhibits an energy barrier almost an order of magnitude smaller than competing directions.[23]Accordingly, we only consider diffusion along this direction in our work. The V_2O_5 structure contains three symmetry inequivalent oxygen sites—namely O(I), O(II), and O(III) (**Figure 6c**). During the hydrogenation process, it is expected that hydrogen atoms initially adhere to oxygen sites that subsequently transform into -OH groups. Additionally, the formation of oxygen vacancies is anticipated since it requires less energy to eliminate -OH groups compared to the removal of oxygen atoms. According to our calculations, neutral oxygen vacancies preferentially occur at O(I) sites which exhibit the smallest defect formation energies of 0.85 eV (under oxygen-poor conditions), in contrast to O(II) and O(III) sites, which have formation energies of 3.05 eV and 3.35 eV, respectively and will not be present in meaningful concentrations (**Figure 6d**). For hydrogenated samples, the formation energies of OH on O(I) and O(II) sites are similar and likely to occur in roughly equal concentrations. O(I) vacancies are found to marginally decrease the barrier for Li^+ diffusion by 2.5 meV and will likely only have a minimal impact on charge storage performance. In contrast, hydrogenation at the OH(I) site significantly reduces the Li^+ ion diffusion barrier by 250 meV, while OH(II) increases the diffusion barrier by 63 meV. (**Figure 6e**). We note that, as both species will be present in equilibrium, the overall effect is likely to be intermediate, resulting in an overall lowering of the Li^+ migration barrier. In conclusion, hydrogenated samples containing oxygen vacancies and -OH sites are expected to demonstrate efficient Li^+ diffusion, resulting in increased capacity and rate capabilities, as well as improved optical and electrical conductivities.

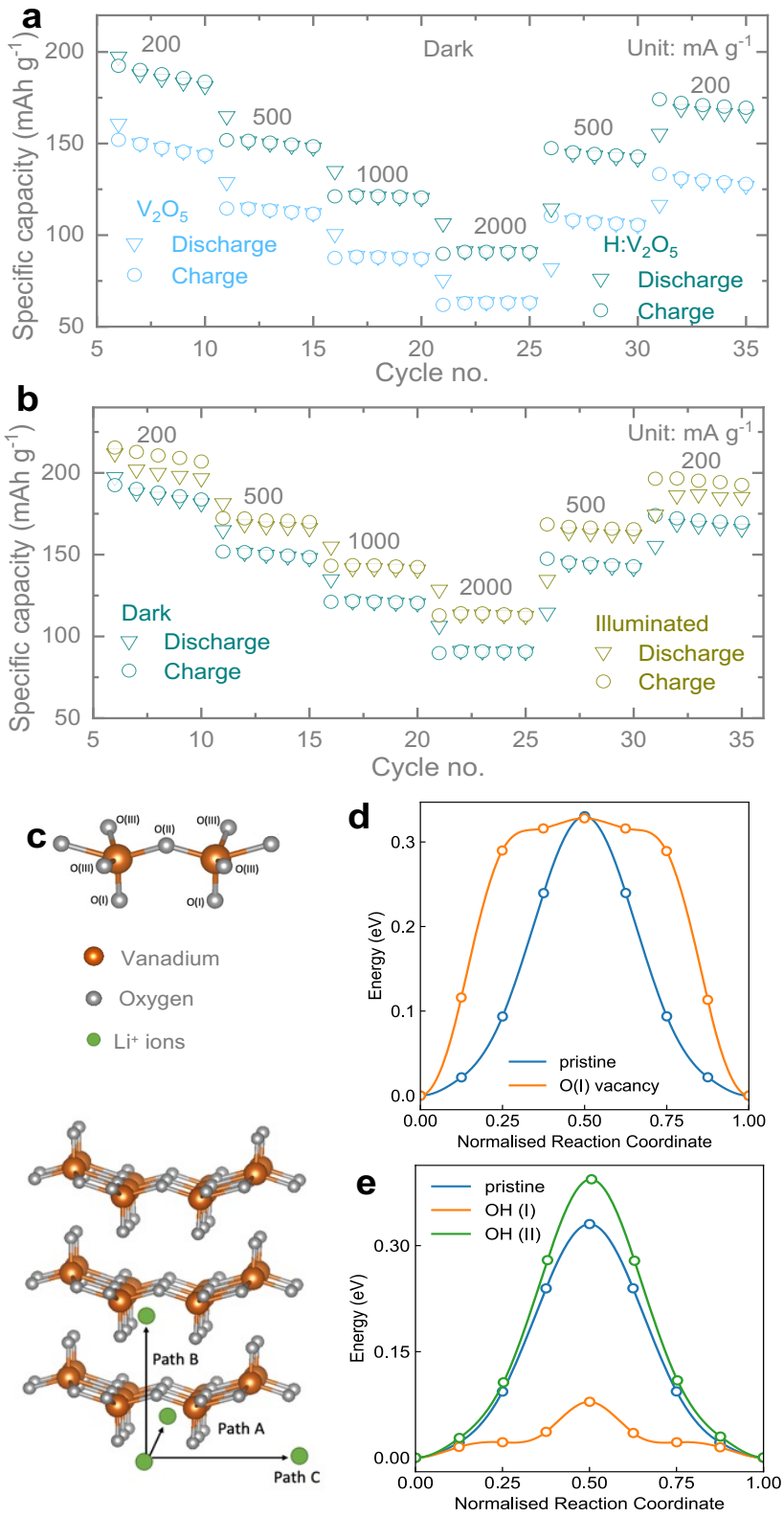

Figure 6. *(a) Comparative rate performance tests of V_2O_5 and H:V_2O_5 in dark showing specific capacities improvements after hydrogenation. (b) Rate performance tests of H:V_2O_5 in dark and illuminated conditions represent improvements of the specific capacities under*

illumination as compared to the dark conditions due to the participation of photo-charges in the charge storage process. (c) Schematics represent the crystal structure of V_2O_5 with possible Li^+ diffusion paths. (d) and (e) Lithium diffusion barrier along path A for V_2O_5 containing (d) oxygen vacancies and (e) hydrogenated oxygen.

This study introduces a novel approach of using hydrogenated V_2O_5 as photo-cathodes for photo-accelerated Li-ion batteries. By introducing oxygen vacancies and -OH groups through hydrogenation, both electrochemical and optical activity are enhanced, leading to improved specific capacities in both dark and light conditions. These results demonstrate the significant impact of such vacancies/defects on promoting Li^+ diffusion, enhancing electronic and ionic conductivity, improving rate performance, and increasing energy storage capacity for photo-accelerated lithium-ion batteries. Overall, this work offers a simple and effective approach for enhancing photo-enhanced energy storage performance and could pave the way for further advancements in photo-accelerated batteries.

ASSOCIATED CONTENT

Supporting Information

The Supporting Information is available

Experimental Section; SAED patterns (**Figure S1**); EDS mappings (**Figure S2**); Raman spectra, schematic and a digital image of a photodetector (**Figure S3**); Digital image of an optical cell (**Figure S**4); CVs in dark (**Figure S5**); CVs of H:V_2O_5 (**Figure S6**); Slopes of redox peaks (**Table S1**); GDC curves (**Figures S7**); Nyquist plots (**Figure S8**); Long-term cycling tests (Figure S10); Variation of OCPs under illumination and discharge in dark (**Figure S11**) and Absolute CV areas and capacity enhancements at different temperatures (**Figure S11**).

AUTHOR INFORMATION

***Corresponding Authors:**

Prof. Ivan P. Parkin – i.p.parkin@ucl.ac.uk

Prof. Michael De Volder – mfld2@cam.ac.uk

Dr. Buddha Deka Boruah – b.boruah@ucl.ac.uk

Notes

The authors declare no competing financial interest.

Acknowledgements

B.D.B. acknowledges support from the EPSRC research grant EP/Y008103/1. A.M.G. was supported by EPSRC Fellowship EP/T033231/1.

References

1. A. Gurung, Q. Qiao, *Joule* **2018**, *2*, 1217-1230.
2. Y. -H. Liu, J. Qu, W. Chang, C. -Y. Yang, H. -J. Liu, X. -Z. Zhai, Y. Kang, Y. -G. Guo, Z. -Z. Yu, *Energy Storage Mater.* **2022**, *50*, 334-343.
3. A. D. Salunke, Chamola, S.; A. Mathieson, B. D. Boruah, M. D. Volder, S. Ahmad, *ACS Appl. Energy Mater.* **2022**, *5*, 7891-7912.
4. B. D. Boruah, A. Mathieson, S. K. Park, X. Zhang, B. Wen, L. Tan, A. Boies, M. D. Volder, *Adv. Energy Mater.* **2021**, *11*, 2100115.
5. B. D. Boruah, A. Mathieson, B. Wen, S. Feldmann, W. M. Dose, M. D. Volder, *Energy Environ. Sci.* **2020**, *13*, 2414-2421.
6. A. Paolella, A. Vijh, A. Guerfi, K. Zaghib, C. Faure, *J. Electrochem. Soc.* **2020**, *167*, 120545.
7. S. Ahmad, C. George, D. J. Beesley, J. J. Baumberg, M. D. Volder, *Nano Lett.* **2018**, *18*, 1856-1862.
8. N. Tewari, S. B. Shivarudraiah, J. E. Halpert, *Nano Lett.* **2021**, *21*, 5578-5585.
9. A. Kumar, P. Thakur, R. Sharma, A. B. Puthirath, P. M. Ajayan, T. N. Narayanan, *Small* **2021**, *17*, 2105029.
10. J. Wang, Y. Wang, C. Zhu, B. Liu, *ACS Appl. Mater. Interfaces* **2022**, *14*, 4071-4078.
11. B. D. Boruah, B. Wen, M. D. Volder, *Nano Lett.* **2021**, *21*, 3527-3532.

12. X. Peng, X. Zhang, L. Wang, L. Hu, S. H. -S. Cheng, C. Huang, B. Gao, F. Ma, K. Huo, P. K. Chu, *Adv. Funct. Mater.* **2016**, *26*, 784-791.
13. B. D. Boruah, B. Wen, S. Nagane, X. Zhang, S. D. Stranks, A. Boies, M. D. Volder, *ACS Energy Lett.* **2020**, *5*, 3132-3139.
14. M. Liao, J. Wang, L. Ye, H. Sun, Y. Wen, C. Wang, X. Sun, B. Wang, H. Peng, *Angew. Chem.* **2020**, *132*, 2293-2298.
15. D. Wu, Y. Zhuang, F. Wang, Y. Yang, J. Zeng, J. Zhao, *Nano Res.* **2021**, 1-8.
16. J.-J. Ye, P.-H. Li, H.-R. Zhang, Z.-Y. Song, T. Fan, W. Zhang, J. Tian, T. Huang, Y. Qian, Z. Hou, N. Shpigel, L.-F. Chen, S. X. Dou, *Adv. Funct. Mater.* **2023**, 2305659, 10.1002/adfm.202305659.
17. L. Liu, T. Yuan, Z. Li, K. Chen, W. Huang, *Electrochimica Acta* **2023**, 439, 141717
18. K. Le, P. V. Pham, C.-L. Dong, et al. *J. Mater. Chem. C* **2022**, 10, 4019.
19. C. Ling, T. Guo, M. Shan, et al. *J. Alloys Compd.* **2019**, 797, 1224-1231.
20. K. Palanisamy, J. H. Um, M. Jeong, W. -S. Yoon, *Sci. Rep.* **2016**, *6*, 31275.
21. D. Y. W. Yu, C. Fietzek, W. Weydanz, K. Donoue, T. Inoue, H. Kurokawa, S. Fujitani, *J. Electrochem. Soc.* **2007**, *154*, A253.
22. R. Pandya, A. Mathieson, B. D Boruah, M. D. Volder, *Nano Lett.* **2023**, 23, 7288-7296.
23. W. Y. Ma, B. Zhou, J. F. Wang, et al. *J. Phys. D: Appl. Phys.* **2013**, 46, 105306.